Supporting Information

Auto-bifunctional Mechanism of Jagged Pt Nanowire for Hydrogen Evolution Kinetics via End-to-End Simulation

Geun Ho Gu[1], Juhyung Lim[1], Chengzhang Wan[2], Tao Cheng[3], Heting Pu[2,] Sungwon Kim[1], Juhwan Noh[1], Changhyeok Choi[1], Juhwan Kim[1], William A. Goddard, III[4*], Xiangfeng Duan[2]*, Yousung Jung[1]*

[1]Department of Chemical and Biomolecular Engineering, Korea Advanced Institute of Science and Technology (KAIST), 291 Daehak-ro 34141, Daejeon 305-335, South Korea

[2]Department of Chemistry and Biochemistry, University of California, 607 Charles E. Young Drive East, Los Angeles, CA 90095-1569, USA.

[3]Institute of Functional Nano & Soft Materials, Soochow University Dushu-Lake Campus, Box 33, 199 Ren'ai Rd, Suzhou Industrial Park, Suzhou, Jiangsu, 215123, P.R. China

[4]Materials and Process Simulation Center, California Institute of Technology, 1200 E California Blvd, Pasadena CA 91125, USA.

Contents

1. Gibbs free energy of reaction and activation

Our model for Gibbs free energy of reaction ($\Delta_r G$) and activation (G_a) for the electrochemical reaction of a proton on the surface depends on three factors: (1) pH, (2) electrode potential and (3) coverage. Here, we summarize the derivation of $\Delta_r G$ and G_a which is an extension of Ref.[1,2] Though we only simulate alkaline chemistry (proton transfer from H_2O), we summarize derivation for acidic conditions (proton transfer from H_3O^+) as well.

1.1. Computational hydrogen electrode

The computational hydrogen electrode (CHE) pioneered by Nørskov and coworkers provides a convenient way to account for the electrode potential for electrochemical reactions.[3] The key for this method is to treat the electrochemical reaction as the removal/addition of a proton and an electron and the usage of the standard hydrogen electrode (SHE) as the reference electrode. For SHE reference electrode, the electrode potential is zero when

$$\mathrm{H^+_{(aq)}} + \mathrm{e^-} \rightarrow \frac{1}{2}\mathrm{H_{2(g)}} \tag{4}$$

is in equilibrium at the $H_{2(g)}$ pressure of 1 bar and pH of 0. Thus, the sum of chemical potentials at each side of the reaction is equal.

$$\mu^\circ_{\mathrm{H^+_{(aq)}}} + \mu^{0V}_{\mathrm{e^-}} = \frac{1}{2}\mu^\circ_{\mathrm{H_{2(g)}}} \tag{5}$$

where $\mu_i^{U_{\mathrm{SHE}}}$ indicates the chemical potential of species *i* at the SHE referenced potential of U_{SHE}. To compute the chemical potential of proton and electron, the equation is rearranged and $\mu^{U_{\mathrm{SHE}}}_{\mathrm{e^-}}$ is added to both side of the equation:

$$\mu^\circ_{\mathrm{H^+_{(aq)}}} + \mu^{U_{\mathrm{SHE}}}_{\mathrm{e^-}} = \frac{1}{2}\mu^\circ_{\mathrm{H_{2(g)}}} - \mathrm{e}U_{\mathrm{SHE}}, \qquad eU_{\mathrm{SHE}} = \mu^{0V}_{\mathrm{e^-}} - \mu^{U_{\mathrm{SHE}}}_{\mathrm{e^-}} \tag{6}$$

To account for the change in the chemical potential due to the pH, $\mu^\circ_{\mathrm{H^+_{(aq)}}} = \mu_{\mathrm{H^+_{(aq)}}} - \ln 10 \; k_{\mathrm{B}}T\mathrm{pH}$ is substituted:

$$\mu_{\mathrm{H}^+_{(\mathrm{aq})}} + \mu_{\mathrm{e}^-}^{U_{\mathrm{SHE}}} = \frac{1}{2}\mu^\circ{}_{\mathrm{H}_{2(\mathrm{g})}} - \mathrm{e}U_{\mathrm{SHE}} - \ln 10 \; k_{\mathrm{B}}T\mathrm{pH} \tag{7}$$

The equation (7) can be conveniently used to calculate the energetics for electrochemical reactions involving proton and electrons using DFT as it only requires the DFT calculation of hydrogen gas.

1.2. Gibbs free energy of reaction

The Volmer reaction, $\mathrm{H}^+_{(\mathrm{aq})} + \mathrm{e}^- + * \rightarrow \mathrm{H}^*$, is the electrochemical adsorption of proton where * indicates the binding site. The $\Delta_{\mathrm{r}}G$ of this reaction is

$$\Delta_{\mathrm{r}}G = \mu_{\mathrm{H}*,i} - \mu_{*,i} - \mu_{\mathrm{H}^+_{(\mathrm{aq})}} - \mu_{\mathrm{e}^-}^{U_{\mathrm{SHE}}} \tag{8}$$

for a site *i*. Substituting the equation (7) to the (8) results in

$$\Delta_{\mathrm{r}}G = \mu_{\mathrm{H}*,i} - \mu_{*,i} - \frac{1}{2}\mu^\circ{}_{\mathrm{H}_{2(\mathrm{g})}} + \mathrm{e}U_{\mathrm{SHE}} + \ln 10 \; k_{\mathrm{B}}T\mathrm{pH} \tag{9}$$

The first three terms are equivalent to the Gibbs free energy of hydrogen adsorption at site *i*,

$$\Delta_{\mathrm{r}}G_{\mathrm{ads},i} = \mu_{\mathrm{H}*,i} - \mu_{*,i} - \frac{1}{2}\mu^\circ{}_{\mathrm{H}_{2(\mathrm{g})}} \tag{10}$$

Thus $\Delta_{\mathrm{r}}G$ for the Volmer reaction is

$$\text{Volmer: } \Delta_{\mathrm{r}}G = \Delta_{\mathrm{r}}G_{\mathrm{ads},i} + \mathrm{e}U_{\mathrm{SHE}} + \ln 10 \; k_{\mathrm{B}}T\mathrm{pH} \tag{11}$$

Similarly, the previous steps can be applied to Heyrovsky reaction, $\mathrm{H}^+_{(\mathrm{aq})} + \mathrm{e}^- + \mathrm{H}^* \rightarrow \mathrm{H}_{2(\mathrm{g})} + *$, resulting in:

$$\text{Heyrovsky: } \Delta_{\mathrm{r}}G = -\Delta_{\mathrm{r}}G_{\mathrm{ads},i} + eU_{SHE} + \ln 10 \; k_B T\mathrm{pH} \tag{12}$$

The Tafel reaction, $\mathrm{H}^* + \mathrm{H}^* \rightarrow \mathrm{H}_{2(\mathrm{g})} + 2*$, does not involve proton and electron, and the electrode potential dependence is trivial,[4] thus it is

$$\text{Tafel: } \Delta_\mathrm{r}G = -\Delta_\mathrm{r}G_{\mathrm{ads},i} - \Delta_\mathrm{r}G_{\mathrm{ads},j} \tag{13}$$

where $\Delta_\mathrm{r}G_{\mathrm{ads},i}$ is the hydrogen adsorption energy for a site *i*. In the case of an alkaline reaction, using that the water dissociation, $\mathrm{H_2O_{(l)}} \rightarrow \mathrm{H^+_{(aq)}} + \mathrm{OH^-_{(aq)}}$, is fast and equilibrated simplifies the derivation.

$$\mu_{\mathrm{H_2O_{(l)}}} = \mu_{\mathrm{H^+_{(aq)}}} + \mu_{\mathrm{OH^-_{(aq)}}} \tag{14}$$

For example, the $\Delta_\mathrm{r}G$ of the basic Volmer reaction, $\mathrm{H_2O_{(l)}} + \mathrm{e^-} + * \rightarrow \mathrm{H^*} + \mathrm{OH^-_{(aq)}}$, is:

$$\Delta_\mathrm{r}G = \Delta_\mathrm{r}G_\mathrm{ads} + \mu_{\mathrm{OH^-_{(aq)}}} - \mu_{\mathrm{H_2O_{(l)}}} - \mu_{\mathrm{e^-}}^{U_\mathrm{SHE}} \tag{15}$$

Substituting the equation (14) to (15) results in (8), thus the $\Delta_\mathrm{r}G$ for the acidic and basic Volmer reaction is the same, which is also the case for the Heyrovsky reaction. The diffusion between site is a non-electrochemical reaction thus the reaction energy is the difference in the adsorption energy:

$$\text{Diffusion: } \Delta_\mathrm{r}G = \Delta_\mathrm{r}G_{\mathrm{ads},i} - \Delta_\mathrm{r}G_{\mathrm{ads},j} \tag{16}$$

where hydrogen atom diffuses from site *j* to site *i*. We note that the coverage effect – the interaction between the adsorbates – are included in the calculation $\Delta_\mathrm{r}G_\mathrm{ads}$ which we discuss in section 6.

1.3. Gibbs free energy of activation

The pH, electrode potential, and coverage effects manifest to the Gibbs free energy by affecting the energy of various states as summarized in Fig. S1 for Volmer reaction. Four states are considered for the acidic and basic condition: (1) $\mathrm{H^+_{(aq)}} + \mathrm{e^-} + *$, (2) $\mathrm{H^+_{(HP)}} + \mathrm{e^-} + *$ (3) transition state, and (4) $\mathrm{H^*}$ for acidic and, (1) $\mathrm{H_2O_{(l)}} + \mathrm{e^-} + *$, (2) transition state (3) $\mathrm{H^*} + \mathrm{OH^-_{(HP)}}$, and (4) $\mathrm{H^*} + \mathrm{OH^-_{(aq)}}$ for alkaline. $\mathrm{H^+_{(aq)}}$ and $\mathrm{OH^-_{(aq)}}$ represents the proton and $\mathrm{OH^-}$ in the bulk liquid as opposed to $\mathrm{H^+_{(HP)}}$ and $\mathrm{OH^-_{(HP)}}$ in the Helmholtz plane. Thus, the energetic

difference between the (HP) and (aq) states represents the energy to shuttle the ion from the bulk liquid to the near-surface. Hence, $H^{+}_{(HP)} + e^{-} + *$ represents the initial state that one would use to compute the barrier of proton transfer reaction using DFT and vice versa for $OH^{-}_{(HP)}$. Another point to note is that, for the acidic proton transfer, since the initial state represents proton in the non-bulk state, DFT calculated TS needs to be referenced from the final state (H*) as it only has water in the Helmholtz plane.

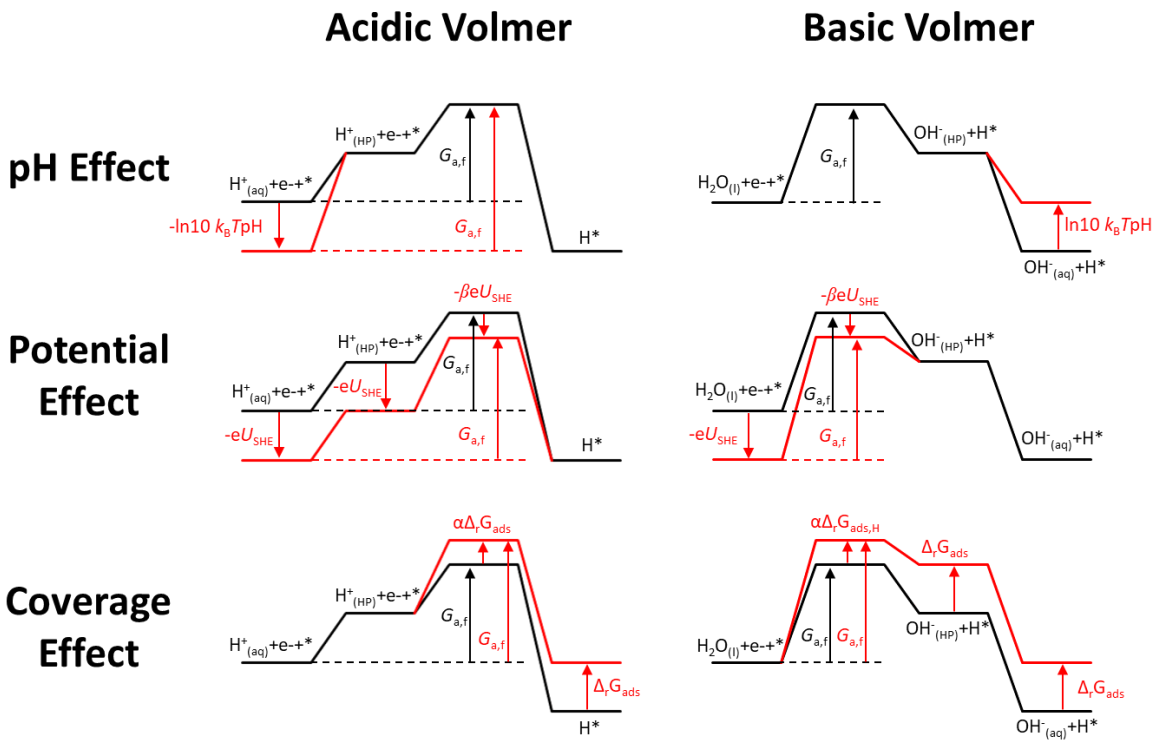

Fig. S1 | pH, potential, and coverage dependent reaction energetics for acidic and basic Volmer reaction. The same strategy can be applied to Heyrovsky reaction.

When the pH changes, only the chemical potential of $H^{+}_{(aq)}$ is affected, as it represents the bulk proton chemical potential. On the other hand, a proton in the Helmholtz plane ($H^{+}_{(HP)}$) represents the particular, rarely observed configuration of water where the proton is near the surface, thus its chemical potential is not affected by the pH. Similarly, for basic reaction, only the chemical potential of $OH^{-}_{(aq)}$ is affected. As a result, only $G_{a,f}$, and $G_{a,r}$ are affected by pH for the reaction involving the proton transfer from hydronium, and water, respectively. Thus, $G_{a,f}(\mathrm{pH}) = G^{\circ}_{a,f} + \ln 10\ k_B T\mathrm{pH}$ for acidic transfer and $G_{a,r}(\mathrm{pH}) = G^{\circ}_{a,r} - \ln 10\ k_B T\mathrm{pH}$ for alkaline transfer.

For the change in the electrode potential, stable states involving electrons are shifted by $-eU_{\mathrm{SHE}}$. In the case of the transition state, energy is only shifted by the amount of the electron transfer involved in the transition state, which is the charge transfer coefficient, β. The energy of the transition state is shifted by $-\beta eU_{\mathrm{SHE}}$. Since the energy of the initial states also shifts for the proton transfer reactions, $G_{\mathrm{a,f}}(U_{\mathrm{SHE}}) = G^{\circ}{}_{\mathrm{a,f}} + (1-\beta)\mathrm{e}U_{\mathrm{SHE}}$.

The change in reaction energy due to the coverage has been well-studied in the field. The increase in coverage increases the energy of H*, $\mu_{\mathrm{H}*}$, by laterally interacting with other adsorbates and ultimately increases $\Delta_{\mathrm{r}}G_{\mathrm{ads}}$ via equation (10). The change in the G_{a} are often described using Brønsted–Evans–Polanyi (BEP) relation: $G_{\mathrm{a,f}} = \alpha\Delta_{\mathrm{r}}G_{\mathrm{ads}} + G^{\circ}{}_{\mathrm{a,f}}$ for Volmer reaction, $G_{\mathrm{a,f}} = \alpha(-\Delta_{\mathrm{r}}G_{\mathrm{ads}}) + G^{\circ}{}_{\mathrm{a,f}}$ for Heyrovsky reaction, $G_{\mathrm{a,f}} = \alpha(-\Delta_{\mathrm{r}}G_{\mathrm{ads},i} - \Delta_{\mathrm{r}}G_{\mathrm{ads},j}) + G^{\circ}{}_{\mathrm{a,f}}$ for Tafel reaction, respectively. For Tafel reaction, *i* and *j* represent the two binding site involved in the Tafel reaction. We discuss in detail in section 6 below how lateral interaction dependent $\mu_{\mathrm{H}*}$is computed.

In summary, the $G_{\mathrm{a,f}}$ are computed by:

$$
\begin{gathered}
\text{Acidic reaction} \\
\text{Volmer: } G_{\mathrm{a,f}} = \alpha(\Delta_{\mathrm{r}}G_{\mathrm{ads},i}) + (1-\beta)\mathrm{e}U_{\mathrm{SHE}} + \ln 10\, k_B T\mathrm{pH} + G^{\circ}{}_{\mathrm{a,f}} \\
\text{Heyrovsky: } G_{\mathrm{a,f}} = \alpha(-\Delta_{\mathrm{r}}G_{\mathrm{ads},i}) + (1-\beta)\mathrm{e}U_{\mathrm{SHE}} + \ln 10\, k_B T\mathrm{pH} + G^{\circ}{}_{\mathrm{a,f}} \\
\text{Basic reaction} \\
\text{Volmer: } G_{\mathrm{a,f}} = \alpha(\Delta_{\mathrm{r}}G_{\mathrm{ads},i}) + (1-\beta)\mathrm{e}U_{\mathrm{SHE}} + G^{\circ}{}_{\mathrm{a,f}} \\
\text{Heyrovsky: } G_{\mathrm{a,f}} = \alpha(-\Delta_{\mathrm{r}}G_{\mathrm{ads},i}) + (1-\beta)\mathrm{e}U_{\mathrm{SHE}} + G^{\circ}{}_{\mathrm{a,f}} \\
\text{Surface reaction} \\
\text{Tafel: } G_{\mathrm{a,f}} = \alpha(-\Delta_{\mathrm{r}}G_{\mathrm{ads},i} - \Delta_{\mathrm{r}}G_{\mathrm{ads},j}) + G^{\circ}{}_{\mathrm{a,f}}
\end{gathered}
\tag{17}
$$

Here, the $G^{\circ}{}_{\mathrm{a,f}}$ is defined at $\Delta_{\mathrm{r}}G_{\mathrm{ads}} = U_{\mathrm{SHE}} = \mathrm{pH} = 0$. The parameters, α, β, and $G^{\circ}{}_{\mathrm{a,f}}$ are retrieved from the previous works on the H/Pt system when possible (Table S1). We could not find α for the basic Volmer and Heyrovsky reaction so we develop the BEP relationship as discussed below. Also, β for the basic Volmer reaction is missing, which we assume is the same as the acidic Volmer reaction.

Table S1 | The parameters and their source for computing $G_{a,f}$ using the equation (2). The bold value in parenthesis indicates a model adjustment to reproduce experimental observation.

Reaction	α	β	$G^\circ_{a,f}$	α source	β source	$G^\circ_{a,f}$ source
Basic Volmer	0.881	0.44	1.270 (**1.173**)	This work	Ref[5a]	Ref[2]
Basic Heyrovsky	0.511	0.59	1.360	This work	Ref[2]	Ref[2]
Tafel	0.462		0.514 (**0.574**)	Ref[5b]		Ref[5b]

[a] β of acidic Volmer reaction from the reference used.
[b] Data sets for (111), (100), (110) are combined to calculate this parameter.

The diffusion-reaction is non-electrochemical and we use the diffusion BEP relationship universal for various adsorbates and elements[6] where

$$G_{a,f} = -0.13G_{IS} - 0.11 \tag{18}$$

Here, G_{IS} represents the binding energy of hydrogen relative to its gaseous state:

$$G_{IS} = \mu_{H*} - \mu_{*} - \mu^\circ_{H_{(g)}} = \Delta_r G_{ads,i} - \mu^\circ_{H_{(g)}} + \frac{1}{2}\mu^\circ_{H_{2(g)}} \tag{19}$$

This method only uses the initial state energy, thus the forward barrier calculated using the binding energy of the initial site and the reverse barrier calculated using the final site are not consistent (i.e. $E_{A,f} \neq E_{A,r} + \Delta_r E$). To ensure thermodynamic consistency, we use the average of the two barriers. We note that the averaging does not affect the result as diffusion reaction is not a rate determining step. Using $-\mu^\circ_{H_{(g)}} + \frac{1}{2}\mu^\circ_{H_{2(g)}} = -2.27$ eV, $G_{a,f}$ for hydrogen diffusion from site *j* to *i* is

$$\text{Diffusion: } G_{a,f} = 0.435\Delta_r G_{ads,i} - 0.565\Delta_r G_{ads,j} + 0.184 \tag{20}$$

2. Density functional theory calculation details

In this work, we use density functional theory (DFT) for (1) computation of $\Delta_r G_{ads}$ to train prediction machine learning model, and (2) development of BEP relationship. Here we summarize the DFT parameter sets used. We perform DFT calculations using the Vienna Ab initio Simulation Package (VASP).[7] Exchange and correlation energies are computed with the revised Perdew, Burke, and Ernzerhof (RPBE) functional,[8] where the core electrons are treated with the projector augmented-wavefunction (PAW) method.[9,10] We use a plane-wave basis set with a 400 eV kinetic energy cutoff for the valence electrons. The Brillouin zone is integrated using a 2×2×1 Monkhorst-Pack k-mesh[11] for the machine learning data (cell size equivalent to 4×4 Pt(111) and Pt(100) slab), and 3×3×1 Monkhorst-Pack k-mesh for the BEP relationship data (*c*(4×4) Pt(111) slab) with a Gaussian Methfessel-Paxton smearing of 0.1.[12] The geometric optimization is performed until the residual force is less than 0.05 eV/Å.

For the calculation of the BEP relationship, the implicit solvation calculations are performed using the generalized Poisson-Boltzmann model as implemented in the VASPsol,[13,14] and the constant electrode potential (CEP) method.[15] The bulk relative permittivity of the water (78.4) is used. The Debye length is set to 3 Å, corresponding to a 1 M concentration of electrolyte (e.g. 1M KOH in our experiment). We add *Q*V correction to address the spurious interaction between the finitely separated the slabs, where the *Q* and V are the net charges of the slab and the negative value of the electrostatic potential of bulk electrolyte, respectively.[16]

3. Brønsted−Evans−Polanyi (BEP) relation development

To build a database for alkaline Volmer and Heyrovsky BEP relations, we employed a three-layer slab of *c*(3×4) with an optimized crystal lattice constant of 3.990 Å. To find the transition state (TS) structure, we used the nudged elastic band to obtain the TS structure[17] which is refined at 0 V vs. SHE using the improved dimer method.[18] We considered Heyrovsky reaction at 0.08, 0.50, 1.00, 1.08, and 1.25 monolayer (ML), and for Volmer reaction at 0.00, 0.25, 0.42, 0.50, 0.58, 0.75, 0.83, 0.92, 1.00 and 1.25 ML. The established BEP relationship is shown in Fig. S2. Here, we only extracted the slope, α, for the $G_{a,f}$ calculation as shown in Table S1 for the reasons we describe below. The obtained slopes for basic Volmer (0.881) and Heyrovsky (0.511) are similar to those obtained for acidic Volmer (0.71) and Heyrovsky reactions (0.59).[5] The slope for the basic Volmer reaction is also similar to the slope of the basic Volmer reaction (0.827) of Liu et al.[19] A recent publication[20] discusses that the CEP method inconsistently describes the electrode potential due to multiple capacitances in the system, which can result in the deviation of $G°_{a,f}$, (intercept). The $G_{a,f}$ obtained from Ref[2] using the constant charge method is 0.42 eV and 1.20 eV for Volmer and Heyrovsky at pH of 14, H* coverage of 0.00 ML and 0.08 ML in *c*(3×4) slab. At the same pH and H* coverage, we obtain 0.804 eV and 1.961 eV using the CEP method, respectively, which deviate significantly. Thus, we use the $G°_{a,f}$ of the constant charge method by referencing to the $G_{a,f}$ at pH 14, and H* coverage of 0.00 ML and 0.08 ML.

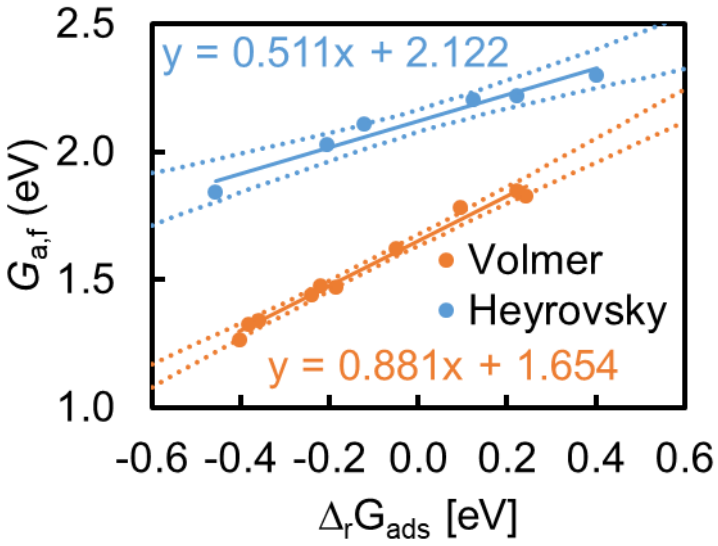

Fig. S2 | The coverage dependent alkaline BEP relationship for Volmer and Heyrovsky. The dotted line indicates the 95 confidence interval of the relations.

4. ReaxFF MD Simulation of the jagged Pt nanowire

To get a realistic structure of jagged Pt nanowire, we implement the force field based methods outlined in Ref[21] which reproduces experimental characterization. Specifically

1. The infinite nanowire (1D system) is constructed based on the fcc Pt crystal structure where the z-axis of the nanowire is along the (111) direction. Along the x- and y-axis there are 13 and 9 Pt atoms. This choice was made to expose (100) facets.
2. The 1D model is replicated to 220 individual unit cells along the z-axis of the wire.
3. 85% of the Pt atoms are randomly selected and removed to simulate the Ni dealloying of 85:15 Ni:Pt nanowire.
4. The conjugate-gradient local relaxation is performed with a fixed-cell using the ReaxFF force field. The maximum change in Cartesian coordinates is limited to 0.1 Å to avoid disruption of the original structure. The nanowire is converged to 4×10^{-6} eV on the energy and 4×10^{-8} eV/Å on the force.
5. Another relaxation is performed with a relaxed cell along the z-direction at a pressure of 1 atm.
6. The NPT Molecular Dynamics (MD) simulation is performed at 343 K for 520 ps (20 ps equilibration followed by a 500 ps run).
7. The least coordinated atoms which would be leached away during ORR cycling are removed.
8. Another NPT Molecular Dynamics (MD) simulation is performed at 343 K for 520 ps (20 ps equilibration followed by a 500 ps run)
9. We relax the final structure using an EMT force field.[22]

Step 3 - 9 is applied to 4×4 Pt(111) and Pt(100) slabs to build a training set for the machine learning model where the number of slab layers is modified so the resulting slab would contain 64 Pt atoms.

5. Gibbs free energy of adsorption prediction via machine learning model development

As the jagged Pt nanowire surface is highly irregular and large, DFT is impractical to predict binding energy. Here, we leverage the machine learning model to make fast predictions on $\Delta_r \mu_{ads}$.

5.1. The Gibbs free energy of adsorption database

We sampled 200 structures for Pt(111) and Pt(100) each from the ReaxFF MD simulation protocol discussed above. We identified five to six binding sites, and their $\Delta_r G_{ads}$ were calculated using the DFT calculations (section 2), resulting in a total of 3413 data points. For geometric optimization, the Pt atom positions were fixed to preserve the geometry, while the H was allowed to move freely.

Our property of interest is $\Delta_r G_{ads} = \mu_{H*} - \mu_* - \frac{1}{2}\mu^\circ{}_{H_{2(g)}}$ as discussed above. Here, μ_* is the DFT calculated empty slab energy, $\mu^\circ{}_{H_{2(g)}}$ is the Gibbs free energy of the hydrogen gas at 1 bar where we account for the translational, rotational, and vibrational degree of freedom, and μ_{H*} is the Gibbs free energy of adsorbed hydrogen where the vibrational degree of freedom has been accounted for. For the vibrational contribution, we used the vibrational frequency obtained from Pt(111) hollow site for all 3413 calculations to reduce the computational cost.

5.2. Data preprocessing for machine learning model training

In this work, we tested the predictive accuracy of four different models: Atom centered symmetric function (ACSF),[23] crystal graph convolutional neural networks (CGCNN),[24] SchNet,[25] and Gaussian Process.[26] For the neural network model, we use the labeled site representation.[27] The labeled site is a simple representation involving labeling the binding site atoms. In this work, we label the binding site atoms by substituting the elements of the hydrogen interacting Pt with an element.[27] To find the binding site atoms, we use the alpha shape to identify top, bridge, and hollow binding sites and designate the binding site closest to the hydrogen as the hydrogen interacting binding site. The alpha shape is a shape formed by tetrahedral polygons of a set of points where a sphere of radius larger than a user-defined size cannot enter the polygons (See Ref[27] for the detailed explanation). By defining the sphere size as the sum of Van der Waals radius of hydrogen and platinum (2.84 Å), we can define the Pt surface where hydrogen gas would not be able to diffuse through without covalently interacting with the Pt surface. After the surface is defined, surface points, connection between points, and

the center of the trigons of tetrahedral polygons become the top, bridge, and hollow site respectively. At this sphere size, the calculated electrochemical surface area (ECSA) is 106.8 m^2/g comparable to the experimental ECSA of 112.9±5.4 m^2/g[28] and 118 m^2/g.[21]

To convert the DFT converged structures to machine (neural network) understandable representation, we focus on the local environment of the binding site similar to those introduced by Chen et al.[29] We used 7.0 Å from the binding site as a cutoff distance based on the first peak at 3.5 Å in the Pt-Pt radial distribution functions in jagged Pt nanowire to create machine learning representation. For the preparation of Gaussian process descriptors, we extracted the distance between the Pt atoms and the binding site for the 12 nearest Pt atoms. We designate this model as the nearest atom distance (NAD).

5.3. Model training and validation

In our previous work, we found that using the average of multiple models reduced model bias and improve the binding energy prediction accuracy, so-called ensemble modeling.[27] Here, we also use ensemble methods for predicting binding energy. To test our model, we hold out 10% of the dataset for testing and performed 5-fold CV using the rest of the data set (Fig. S3). Thus, we form five models for each method, and predictions are made to the 10% test set where the predictions are averaged before comparing with the true binding energies. As shown in Table S2, using the average prediction of five models shows higher accuracy than using one model alone. We also tested averaging the predictive accuracy of multiple model frameworks (e.g., ACSF and CGCNN), but the improvement was minimal. Here, we find that the ensemble of ACSF models shows the best performance with a mean absolute error of 0.043 eV, thus we use ACSF for predicting binding energies.

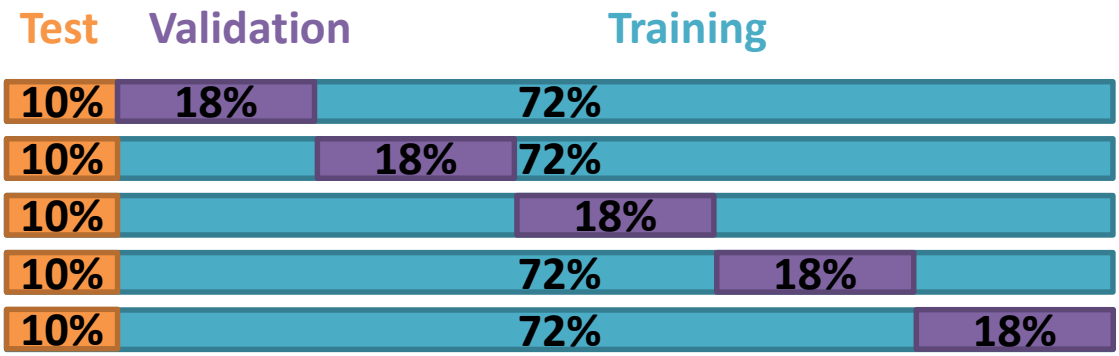

Fig. S3 | Test, validation training split visualization for the 5-fold cross-validation used in this work.

Table S2 | Out-of-sample (test) set error statistics for various models considered. The red values indicate the lowest value within the columns. The plus sign indicates the combination of multiple machine learning methods. NAD is the Gaussian process method that uses the distance of Pt atoms nearest to the binding site as descriptors.

Model	Mean absolute error (eV)	Root mean squared error (eV)	Max absolute error (eV)
ACSF*	0.046	0.060	0.227
NAD*	0.057	0.073	0.283
CGCNN*	0.057	0.072	0.267
SchNet*	0.069	0.088	0.306
ACSF	**0.043**	**0.056**	0.221
NAD	0.057	0.073	0.287
CGCNN	0.056	0.071	0.243
SchNet	0.068	0.088	0.336
ACSF+NAD	0.046	0.059	0.211
ACSF+CGCNN	0.044	0.057	0.214
ACSF+SchNet	0.049	0.064	0.202
NAD+CGCNN	0.051	0.066	0.243
NAD+SchNet	0.057	0.074	0.279
CGCNN+SchNet	0.057	0.074	0.240
ACSF+NAD+CGCNN	0.046	0.059	0.207
ACSF+NAD+SchNet	0.049	0.063	0.231
ACSF+CGCNN+SchNet	0.049	0.063	**0.201**
NAD+CGCNN+SchNet	0.054	0.069	0.252
ACSF+NAD+CGCNN+SchNet	0.048	0.062	0.223

*Best model out of five

5.4. Application to Jagged Pt Nanowire

To apply our model to the various Pt surfaces considered for KMC simulation, the alpha shape strategy discussed in section 5.2 is applied to the force field obtained Pt surfaces to find binding site atoms. Then, the site labeling and local environment pruning (see section 5.2.) are applied to predict binding energies.

6. Coverage effect model development

To apply the coverage effect introduced in Section 1, we need to model the lateral interaction, the repulsive interaction between the adsorbates. Here, we derive the hydrogen-hydrogen interaction energy from the experiments using the mean-field Ising (cluster expansion) model. We collected differential energy of adsorption for Pt(111), Pt(100), and Pt(110) from three different studies[30-32] and plotted it against the hydrogen surface density as shown in Fig. S4.

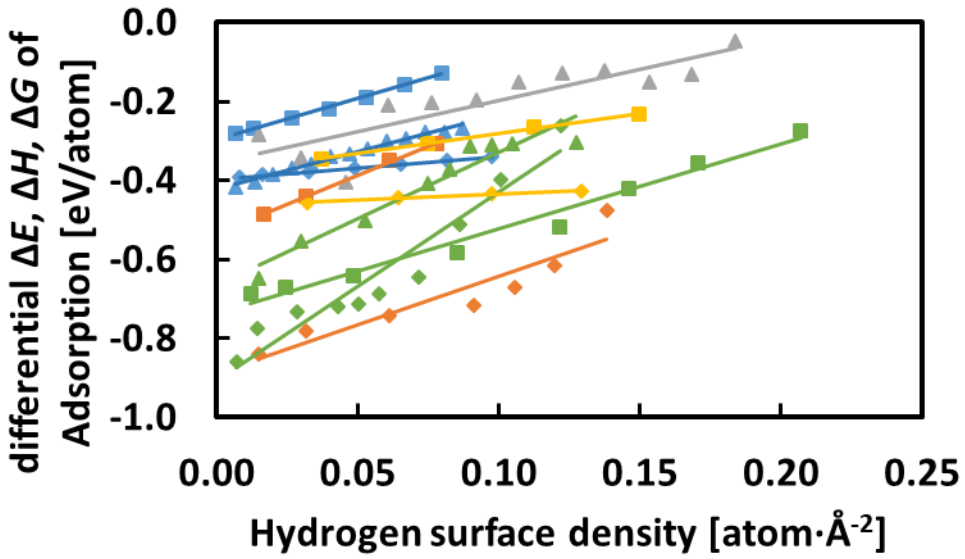

Fig. S4 | Differential energy, enthalpy, and Gibbs free energy of adsorption vs, the hydrogen surface for Pt(111) (Square), Pt(100) (diamond), and Pt(110) (triangle). Blue, gray, yellow, orange, and green colors from Ref,[30] Ref,[33] Ref,[34] Ref,[31] and Ref,[32] respectively. Y-axis value of Blue is Gibbs free energy (ΔG), those of gray and yellow are electronic energy (ΔE), and those of orange and green are enthalpy (ΔH) of adsorption.

Here, the change in adsorption energy (the slope in the figure) is fairly consistent between different surfaces and studies when plotted against the hydrogen surface density (2.1 ± 0.76 eV·Å^2·atom^{-2}), thus we use this information to estimate hydrogen-hydrogen lateral interaction. It has been shown that the nearest neighbor pair-wise interaction (Ising model) is sufficient to reproduce cyclo voltammetry data[34] thus we parameterize the Ising model using the experimental data.

Using the Ising model formulation, system energy can be written as

$$\mathrm{E} = \sum_{i}^{N} E_i \sigma_i + J \sum_{<i,j>}^{N} \sigma_i \sigma_j \qquad (21)$$

where E_i is the binding energy of site i, and σ_i is the occupancy where 0 is the unoccupied, and 1 is the occupied site, N is the number of sites. In the case of KMC simulation, equation (21) can be directly used as E_i and σ_i are rigorously calculated. We estimate J from Fig. S4 by using mean-field theory to correlate to the experimental result. σ_i can be written as the fluctuation from its mean value, m.

$$\mathrm{E} = \sum_i^N E_i\sigma_i + J\sum_{<i,j>}^N (m_i + d\sigma_i)\big(m_i + d\sigma_j\big) \tag{22}$$

where $d\sigma_i = \sigma_i - \mathrm{m}_i$, the fluctuation. Expanding the equation:

$$\mathrm{E} = \sum_i^N E_i\sigma_i + J\sum_{<i,j>}^N \big(m_i m_j + m_i d\sigma_j + m_j d\sigma_i + d\sigma_i d\sigma_j\big) \tag{23}$$

The last term is the product of two fluctuations, which is negligible at the limit of a large surface. Also, we assume that every site is equivalent in terms of lateral interaction for the simple parameterization (i.e., $m=m_i=m_j$). By accounting for these factors, and substituting the $d\sigma_i = \sigma_i - \mathrm{m}_i$,

$$\begin{aligned}\mathrm{E} &= \sum_i^N E_i\sigma_i + J\sum_{<i,j>}^N (m^2 + 2m(\sigma_i - m)) \\ &= \sum_i^N E_i\sigma_i + J\sum_{<i,j>}^N (-m^2 + 2m\sigma_i)\end{aligned} \tag{24}$$

The summation over <i,j> can be written as $\sum_{<i,j>}^N = 1/2\sum_i^N\sum_{j\in nn(i)}$ where ½ is to account for the double-counting, and nn(i) indicates the nearest-neighbor of i. Simplifying this expression result in:

$$\mathrm{E} = \sum_i^N E_i\sigma_i - \frac{Jm^2Nz}{2} + Jmz\sum_i^N \sigma_i \tag{25}$$

where N is the total number of sites, and z is the coordination number, i.e. the number of adjacent sites. This is the mean-field theory solution to the Ising model. Equation (25) represents the energy of the entire surface and Fig. S4 is adsorption energy per site differentiated by hydrogen surface density $\rho_{\mathrm{H}} = \frac{N_{\mathrm{H}}}{N}\rho_{\mathrm{S}}$, where $N_{\mathrm{H}} = \sum_i^{\mathrm{N}} \sigma_i$ is the number of hydrogen, and ρ_{S} is the surface site density. Dividing the Equation (25) by N_{s} to get energy per site and using that $m = \frac{N_S}{N}$, and E_i is consistent for single facet (=E_0), Equation (25) simplifies to:

$$\frac{E}{N_{\mathrm{H}}} = E_0 + \frac{Jz}{2}\frac{\rho_{\mathrm{H}}}{\rho_{\mathrm{S}}} \tag{26}$$

Taking the first derivative results in the slope of Fig. S4:

$$\frac{dE/N_{\mathrm{H}}}{d\rho_{\mathrm{H}}} = \frac{Jz}{2\rho_{\mathrm{S}}} \tag{27}$$

Here, we use ρ_{S} equal to 0.14 atom/Å^2, the average of 0.15, 0.13, and 0.14 atom/Å^2 for (111), (100), and (110) – (1×2) respectively. In all three surfaces, *z* is 6, by considering only the sites that are filled by hydrogen before the over-saturation (>1 ML), resulting in J = 0.098 ± 0.035 eV. The sites on nanowire may have more than 6 nearest neighbor sites thus local oversaturation is plausible, but the oversaturation is not observed until very low potential which is not considered in this study. The distances between sites in single crystal surfaces are all within 2.78 Å, thus, for nanowire, sites within 2.78 Å radius are identified for each site and are considered nearest-neighbors for lateral interactions.

To apply this model to our system, $\mu_{\mathrm{H}*}$ can be further expanded:

$$\mu_{\mathrm{H}*} = \mu^{\circ}{}_{\mathrm{H}*} + J\Delta n_{\mathrm{H-H}} \tag{28}$$

where $\mu^{\circ}{}_{\mathrm{H}*}$ indicates the energy of adsorbed hydrogen at the zero-coverage limit, $\Delta n_{\mathrm{H-H}}$ is the change in the number of H-H interactions (number of hydrogen pairs are within 2.78 Å) between the final and initial states. The zero-coverage limit is the coverage where lowering the coverage no-longer changes the adsorption energy. For the Gibbs free energy of adsorption

database we have built, the hydrogen atoms are sufficiently far apart across the periodic boundary that the lateral interaction is not felt across the periodic boundary. For the KMC simulation, graph theory can be used to compute $\Delta n_{\mathrm{H-H}}$.

7. Graphic theoretical kinetic Monte Carlo simulation

The graphic theoretical kinetic Monte Carlo provides site-resolved insights into catalysis that are otherwise not possible using the mean-field microkinetic models and experiments. In this method, each binding site is explicitly defined and a reaction is simulated one at a time, thus provides a high-resolution picture into catalysis as shown in Fig. S5 with a Pt(111) example. A great review is provided in ref.[35] In this section, we summarize the methodology for Pt surface graph generation, the graphical definition of reactions, the Kinetic Monte Carlo algorithm, and the model validation and adjustments.

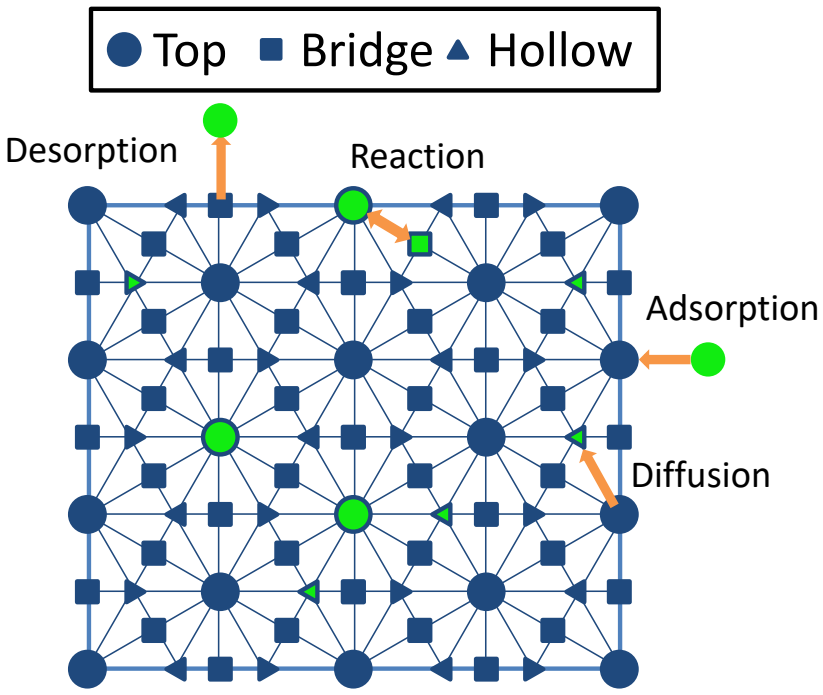

Fig. S5 | An Pt(111) example of a graph theoretical kinetic Monte Carlo. The green and blue fill represents the adsorbate and the empty binding sites. In graphical kinetic Monte Carlo reactions are simulated one at a time with the site-resolved picture to provide catalytic insights.

7.1. Pt surface graph generation, and reaction graph definition

To generate the surface graph, we use the alpha shape procedure introduced in section 5.2. From the ReaxFF, we sampled the jagged Pt nanowire's structure, and alpha shape is used to convert its surface the polygonal shape, where the points are the atoms/top sites, the edges of the polygons are the bridge site and the center of the triangle is the hollow site. The Volmer

and Heyrovsky reactions are available to all sites, whereas Tafel and diffusion reactions are defined for a pair of adjacent sites as shown in Fig. S6.

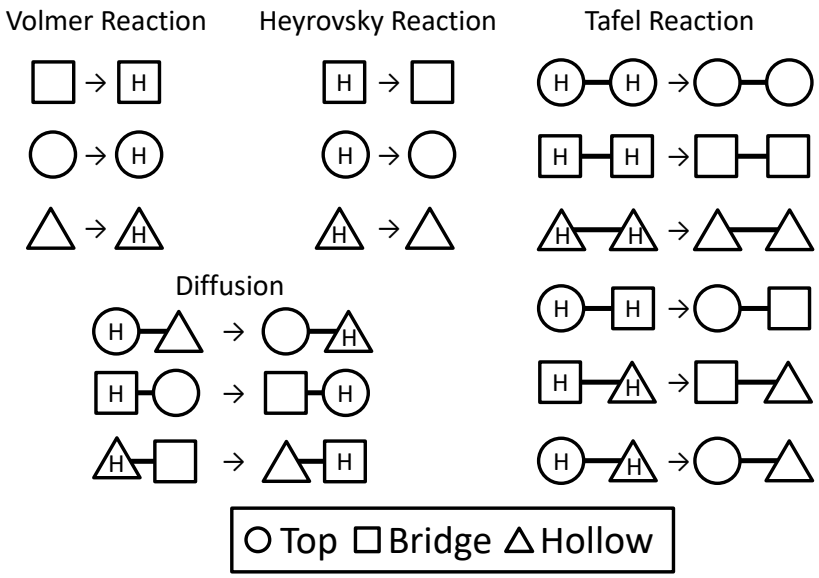

Fig. S6 | The change in the surface graph for each reaction type.

7.2. Kinetic Monte Carlo algorithm

We used the graph-theoretical kinetic Monte Carlo algorithm as outlined in Stamatakis et al[35] and we also implemented the reaction scaling method by Núñez et al[36] to speed up the simulation. Reaction constants are calculated using the transition state theory and thermodynamic equilibrium:

$$k_{\mathrm{f}} = \frac{k_{\mathrm{b}}T}{h}\exp\left(\frac{-G_{\mathrm{a,f}}}{k_{\mathrm{b}}T}\right)$$
$$k_{\mathrm{r}} = \frac{k_{\mathrm{f}}}{K} \qquad (29)$$
$$K = \exp\left(\frac{-\Delta_{\mathrm{r}}G}{k_{\mathrm{b}}T}\right)$$

The pseudo-code for the KMC algorithm is provided below:

0. Start
1. Initialize all reaction constants
2. Run parallel KMC simulations until 1000 events
3. Rescale the fast equilibrated reactions as described in Ref[36]
4. Set the termination time for the next run to be twice the first run

5. Run parallel KMC simulation until the termination time
6. Rescale the fast equilibrated reactions
7. Repeat 4 – 6 until the system reaches the steady-state (which we define as when the noise in the current density is within ~10%)

We used the rejection-free KMC algorithm as it is the fastest algorithm for our system.

7.3. Model validation, degree of rate control analysis, uncertainty, and adjustments

The followings are the supplementary figures and tables regarding the model validation.

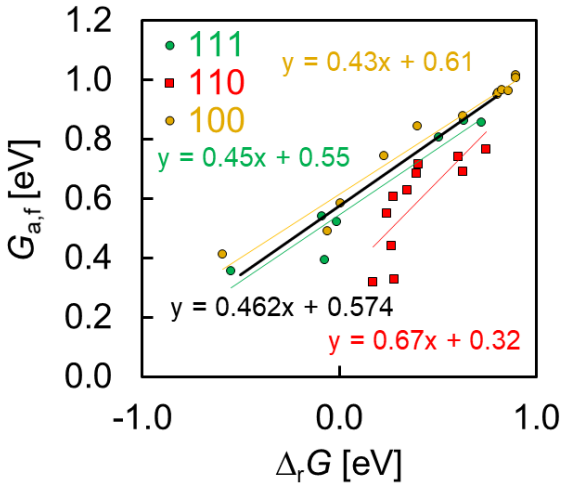

Fig. S7 | Tafel reaction BEP trends obtained from ref[5] for Pt(111) (green), Pt(110) (red), and Pt(100) (Yellow). In our model, we use the black trend line which falls well within the distribution of the data.

Table S3 | Higher and lower bounds of reproduced measurements based on 95% confidence intervals of sensitive parameters. BV and M indicate Butler-Volmer and micropolarization fitting, respectively.

	Lateral Interaction (J)	Tafel BEP relation	Volmer BEP relation
Tafel Slope (mV/dec)	72.9 (72.5, 77.5)	72.9 (71.1, 85.7)	72.9 (72.1, 75.5)
BV i_0 (mA cm^{-2})	0.81 (0.60, 1.12)	0.81 (0.62, 0.83)	0.81 (0.36, 1.72)
BV β	0.46 (0.45, 0.48)	0.46 (0.45, 0.52)	0.46 (0.46, 0.47)
M i_0 (mA cm^{-2})	0.83 (0.60, 1.12)	0.83 (0.63, 0.85)	0.83 (0.40, 1.72)
Bifunctional Gain	4.61 (3.10, 4.81)	4.61 (2.78, 6.12)	4.61 (3.02, 4.67)

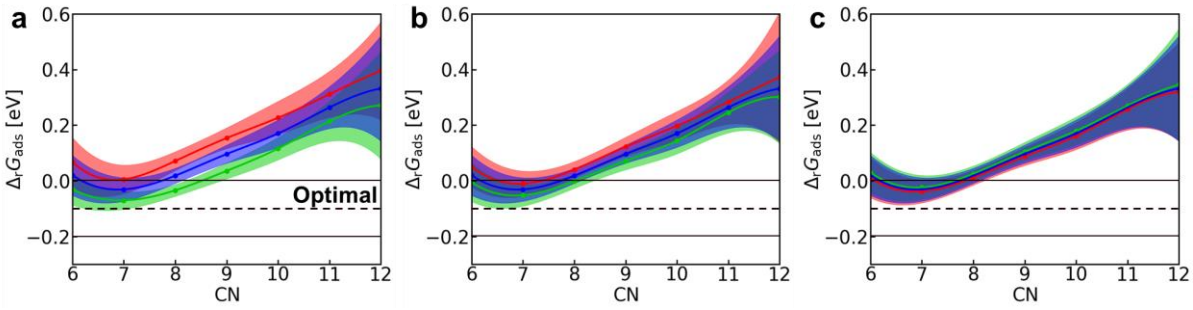

Fig. S8 | Change in $\Delta_r G_{ads}$ vs. CN within the 95 confidence interval of (**a**) J (HH cluster interaction energy) (**b**) Tafel barriers and (**c**) Volmer barriers. The blue, red, and green colors indicate the norm, upper, and lower interval. Overall the conclusion that Pt atom with lower CN is the active centers remains the same.

7.4. Effect of jagged Pt nanowire length

We made 46.1 nm nanowire using the force field approach, and we cut the wire at various lengths to produce the Figures in this study. To check the validity using a shorter wire, we plot the zero coverage Gibbs free energy of adsorption, $\Delta_r G_{ads,0}$, at various lengths, as shown in Fig. S9. The larger wire length results in a smoother normal distribution. We test the normality of the distribution using a 2-sided chi-squared probability for skewness and kurtosis, which is all below 0.296% of 2.3 nm signifying their normality (Table S4). We find that the current density is within 10% of each other for all tested lengths (2.3, 4.6, 9.2, and 23.0 nm) of the wire (Table S4). At the minimum, we used a 2.3 nm wire length to produce results that are sufficient to reproduce the macroscopic behavior.

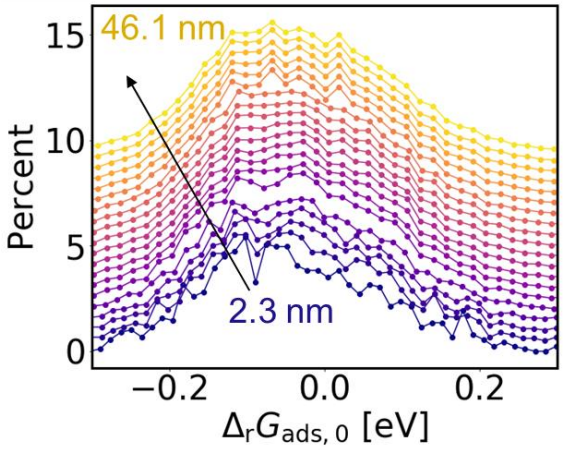

Fig. S9 | The distribution of zero coverage Gibbs free energy of adsorption, $\Delta_r G_{ads,0}$, for various length of the jagged Pt nanowire (with an offset of 0.5 for each increase in length)

Table S4 | A 2-sided chi-squared probability for normality (skewness and kurtosis test) for zero coverage Gibbs free energy of adsorption, $\Delta_r G_{ads,0}$ of jagged Pt nanowire at various length, L at pH 14, 298K and -0.05 V vs. RHE and 1 bar H_2

L (nm)	$\Delta_r G_{ads,0}$ normality X^2	Steady State i (mA cm^{-2})	Output Figures and Tables
2.3	2.96×10^{-3}	1.76 ± 0.08	Fig. 2, Table S3, Fig. S8
4.6	2.28×10^{-4}	1.71 ± 0.02	Fig. 4
6.9	3.18×10^{-4}		
9.2	2.08×10^{-5}	1.75 ± 0.02	Fig. 3bc, Fig. 6
11.5	6.01×10^{-8}		
13.8	8.64×10^{-8}		
16.1	5.54×10^{-9}		
18.4	2.76×10^{-9}		
20.7	5.14×10^{-11}		
23.0	2.64×10^{-12}	1.96 ± 0.02	Fig. 3a, Fig. 7, Fig. S10
25.4	3.52×10^{-14}		
27.7	2.84×10^{-15}		
30.0	2.53×10^{-18}		
32.3	1.39×10^{-19}		
34.6	4.84×10^{-19}		
36.9	9.56×10^{-23}		
39.2	3.24×10^{-24}		
41.5	4.19×10^{-26}		
43.8	2.28×10^{-28}		
46.1	7.84×10^{-26}		

8. Experimental details

8.1. Synthesis of PtNi alloy nanowire on carbon

All chemicals were purchased from Sigma-Aldrich unless otherwise specified. In a typical synthesis, 20 mg $Pt(acac)_2$ and 40 mg $Ni(acac)_2$ were mixed with 130 mg glucose, 1.7 mg $W(CO)_6$ and 60 mg PVP (molecular weight: 40000) in a glass vial, with 3 ml of oleylamine and 2 mL octadecene as co-solvent. The mixture was heated to 140 °C for 6 h to form Pt–NiO core–shell nanowires. The resulting nanowires were collected via centrifuge at 7,000 r.p.m. for 20 min. After loading the nanowires on pretreated Vulcan 72 carbon black, the catalysts were then annealed under 450 °C in argon/hydrogen (97:3) atmosphere for 12 h to obtain the PtNi alloy nanowires supported on carbon black.

8.2. Electrochemical dealloying of PtNi nanowire to synthesize jagged Pt nanowire

The ink was prepared by dispersing 1 mg catalysts and 10 uL Nafion solution in 1 mL ethanol using sonication. 10 uL ink was then dropcasted on the rotating disk electrode (RDE: 0.196 cm^2) as the working electrode. The Ag/AgCl electrode and the Pt wire were used as the reference electrode and the counter electrode, respectively. The potential of the reference electrode has been pre-calibrated under 1 atmosphere H_2. An electrochemical dealloying process was performed via 200 cyclic voltammetry (CV) cycles of working electrode between 0.05 V and 1.10 V versus RHE in 0.1 M $HClO_4$ at a scan rate of 100 mV/s to completely remove the nickel species. N_2 gas was continuously purged to remove the O_2 from the electrolyte. After complete dealloying, the remained Pt surface then became a jagged surface which has been characterized by previous works.

8.3. Electrochemical hydrogen evolution/oxidation reaction test

After dealloying, the working electrode was carefully washed using deionized water and transferred into 1 M KOH electrolyte (N_2) purge and scan CV from 0.05 V to 1.10 V vs. RHE at a scan rate of 100 mV/s until the CV is stable. The reference electrolyte and counter electrode used in 1 M KOH were Hg/HgO electrode and graphite rod electrode, respectively. The HER/HOR tests were then performed via linear scan voltammetry (LSV) from -0.05 V to 0.10 V vs. RHE at a scan rate of 10 mV/s with continuous H_2 purging. All the presented HER/HOR polarization curves and following data analysis are *iR*-corrected.

8.4. Obtaining exchange current density, symmetric factor, and Tafel slope from the HER/HOR Polarization curve

After obtaining the HER/HOR polarization curve, the HOR branch was corrected by Koutecky–Levich equation (eq. (30)), where j is the current density collected on the working electrode and j_k is the kinetic current density and j_d is the H_2-diffusion limiting current density. The corrected HER/HOR polarization curve was then fitted from -0.05 V to 0.05 V using Butler−Volmer equation (eq. (31)), and fitted from -0.01 V to 0.01 V using micropolarization linear fitting (eq. (32)), to get symmetric factor β and the exchange current density $j_{0,\,RDE}$ (normalized by RDE geometric surface area). Here, R is the universal gas constant, T is the temperature in Kelvin, F is the Faraday's constant, and η is the overpotential. The Tafel slope was then directly measured from the Butler−Volmer plot.

$$\frac{1}{j} = \frac{1}{j_k} + \frac{1}{j_d} \tag{30}$$

$$j_k = j_{0,RDE} \times \left(e^{\frac{\beta F \eta}{RT}} - e^{\frac{(\beta-1)F\eta}{RT}}\right) \tag{31}$$

$$j = j_{0,RDE} \times \frac{\eta F}{RT} \tag{32}$$

After obtaining $j_{0,\,RDE}$, the intrinsic exchange current density $i_{0,\,\mathrm{ECSA}}$ was determined by the following simple calculation (33). Here the A_{Hupd} is the hydrogen underpotential deposition area of the jagged Pt nanowires, which was determined from its CV plot in 1 M KOH.

$$i_0 = j_{0,RDE} \frac{0.196}{A_{Hupd}} \tag{33}$$

9. Supplementary Figures

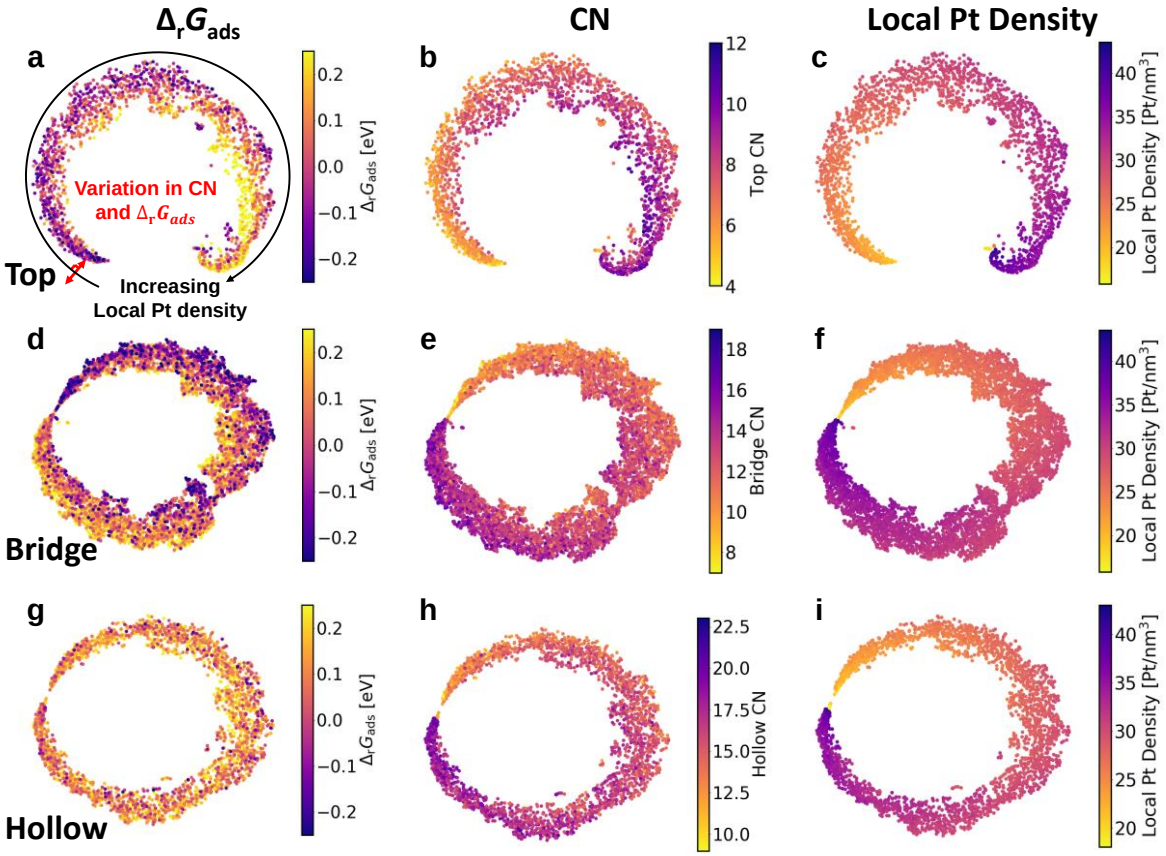

Fig. S10 | Visualization of the optimized latent coordinate of sites based on the similarity between sites for each site type: top (**a**, **b**, **c**), bridge (**d**, **e**, **f**), and hollow sites (**g**, **h**, **i**). The colors represent $\Delta_r G_{ads}$ (**a**, **d**, **g**), coordination number (CN) (**b**, **e**, **h**), and local Pt density (**c**, **f**, **i**). The t-SNE optimized sites' latent coordinates based on the CN and the local Pt density. The examination shows that CN is correlated to the $\Delta_r G_{ads}$.

10. Reference

(1) Lindgren, P.; Kastlunger, G.; Peterson, A. A. A Challenge to the G ~ 0 Interpretation of Hydrogen Evolution. *ACS Catal.* **2020**, *10*, 121.

(2) Lamoureux, P. S.; Singh, A. R.; Chan, K. pH Effects on Hydrogen Evolution and Oxidation over Pt(111): Insights from First-Principles. *ACS Catal.* **2019**, *9*, 6194.

(3) Nørskov, J. K.; Rossmeisl, J.; Logadottir, A.; Lindqvist, L.; Kitchin, J. R.; Bligaard, T.; Jónsson, H. Origin of the Overpotential for Oxygen Reduction at a Fuel-Cell Cathode. *J. Phys. Chem. B* **2004**, *108*, 17886.

(4) Fang, Y.-H.; Wei, G.-F.; Liu, Z.-P. Catalytic Role of Minority Species and Minority Sites for Electrochemical Hydrogen Evolution on Metals: Surface Charging, Coverage, and Tafel Kinetics. *J. Phys. Chem. C* **2013**, *117*, 7669.

(5) Skúlason, E.; Tripkovic, V.; Björketun, M. E.; Gudmundsdóttir, S.; Karlberg, G.; Rossmeisl, J.; Bligaard, T.; Jónsson, H.; Nørskov, J. K. Modeling the Electrochemical Hydrogen Oxidation and Evolution Reactions on the Basis of Density Functional Theory Calculations. *J. Phys. Chem. C* **2010**, *114*, 18182.

(6) Peng, G.; Mavrikakis, M. Adsorbate Diffusion on Transition Metal Nanoparticles. *Nano Lett.* **2015**, *15*, 629.

(7) Kresse, G.; Furthmüller, J. Efficient iterative schemes for *ab initio* total-energy calculations using a plane-wave basis set. *Phys. Rev. B* **1996**, *54*, 11169.

(8) Hammer, B.; Hansen, L. B.; Nørskov, J. K. Improved adsorption energetics within density-functional theory using revised Perdew-Burke-Ernzerhof functionals. *Phys. Rev. B* **1999**, *59*, 7413.

(9) Blöchl, P. E. Projector augmented-wave method. *Phys. Rev. B* **1994**, *50*, 17953.

(10) Kresse, G.; Joubert, D. From ultrasoft pseudopotentials to the projector augmented-wave method. *Phys. Rev. B* **1999**, *59*, 1758.

(11) Monkhorst, H. J.; Pack, J. D. Special points for Brillouin-zone integrations. *Phys. Rev. B* **1976**, *13*, 5188.

(12) Methfessel, M.; Paxton, A. T. High-precision sampling for Brillouin-zone integration in metals. *Phys. Rev. B* **1989**, *40*, 3616.

(13) Mathew, K.; Kolluru, V. C.; Mula, S.; Steinmann, S. N.; Hennig, R. G. Implicit self-consistent electrolyte model in plane-wave density-functional theory. *J. Chem. Phys.* **2019**, *151*, 234101.

(14) Mathew, K.; Sundararaman, R.; Letchworth-Weaver, K.; Arias, T.; Hennig, R. G. Implicit solvation model for density-functional study of nanocrystal surfaces and reaction pathways. *J. Chem. Phys.* **2014**, *140*, 084106.

(15) Van den Bossche, M.; Skúlason, E.; Rose-Petruck, C.; Jónsson, H. Assessment of Constant-Potential Implicit Solvation Calculations of Electrochemical Energy Barriers for H2 Evolution on Pt. *J. Phys. Chem. C* **2019**, *123*, 4116.

(16) Van den Bossche, M.; Skúlason, E.; Rose-Petruck, C.; Jónsson, H. Addition to "Assessment of Constant-Potential Implicit Solvation Calculations of Electrochemical Energy Barriers for H2 Evolution on Pt". *J. Phys. Chem. C* **2019**, *123*, 15875.

(17) Henkelman, G.; Jónsson, H. Improved tangent estimate in the nudged elastic band method for finding minimum energy paths and saddle points. *J. Chem. Phys.* **2000**, *113*, 9978.

(18) Heyden, A.; Bell, A. T.; Keil, F. J. Efficient methods for finding transition states in chemical reactions: Comparison of improved dimer method and partitioned rational function optimization method. *J. Chem. Phys.* **2005**, *123*, 224101.

(19) Liu, L.; Liu, Y.; Liu, C. Enhancing the Understanding of Hydrogen Evolution and Oxidation Reactions on Pt(111) through Ab Initio Simulation of Electrode/Electrolyte Kinetics. *J. Am. Chem. Soc.* **2020**, *142*, 4985.

(20) Gauthier, J. A.; Dickens, C. F.; Heenen, H. H.; Vijay, S.; Ringe, S.; Chan, K. Unified Approach to Implicit and Explicit Solvent Simulations of Electrochemical Reaction Energetics. *J. Chem. Theory Comput.* **2019**, *15*, 6895.

(21) Li, M.; Zhao, Z.; Cheng, T.; Fortunelli, A.; Chen, C.-Y.; Yu, R.; Zhang, Q.; Gu, L.; Merinov, B. V.; Lin, Z.; Zhu, E.; Yu, T.; Jia, Q.; Guo, J.; Zhang, L.; Goddard, W. A.; Huang, Y.; Duan, X. Ultrafine jagged platinum nanowires enable ultrahigh mass activity for the oxygen reduction reaction. *Science* **2016**, *354*, 1414.

(22) Jacobsen, K. W.; Stoltze, P.; Nørskov, J. K. A semi-empirical effective medium theory for metals and alloys. *Surf Sci.* **1996**, *366*, 394.

(23) Behler, J. Atom-centered symmetry functions for constructing high-dimensional neural network potentials. *J. Chem. Phys.* **2011**, *134*, 074106.

(24) Xie, T.; Grossman, J. C. Crystal Graph Convolutional Neural Networks for an Accurate and Interpretable Prediction of Material Properties. *Phys. Rev. Lett.* **2018**, *120*, 145301.

(25) Schütt, K. T.; Sauceda, H. E.; Kindermans, P. J.; Tkatchenko, A.; Müller, K. R. SchNet – A deep learning architecture for molecules and materials. *J. Chem. Phys.* **2018**, *148*, 241722.

(26) Rasmussen, C. E. In *Advanced Lectures on Machine Learning: ML Summer Schools 2003, Canberra, Australia, February 2 - 14, 2003, Tübingen, Germany, August 4 - 16, 2003, Revised Lectures*; Bousquet, O., von Luxburg, U., Rätsch, G., Eds.; Springer Berlin Heidelberg: Berlin, Heidelberg, 2004, p 63.

(27) Gu, G. H.; Noh, J.; Kim, S.; Back, S.; Ulissi, Z. W.; Jung, Y. Practical Deep-Learning Representation for Fast Heterogeneous Catalyst Screening. *J. Phys. Chem. Lett.* **2020**, *11*, 3185.

(28) Li, M.; Duanmu, K.; Wan, C.; Cheng, T.; Zhang, L.; Dai, S.; Chen, W.; Zhao, Z.; Li, P.; Fei, H.; Zhu, Y.; Yu, R.; Luo, J.; Zang, K.; Lin, Z.; Ding, M.; Huang, J.; Sun, H.; Guo, J.; Pan, X.; Goddard, W. A.; Sautet, P.; Huang, Y.; Duan, X. Single-atom tailoring of platinum nanocatalysts for high-performance multifunctional electrocatalysis. *Nat. Catal.* **2019**, *2*, 495.

(29) Chen, Y.; Huang, Y.; Cheng, T.; Goddard, W. A. Identifying Active Sites for CO2 Reduction on Dealloyed Gold Surfaces by Combining Machine Learning with Multiscale Simulations. *J. Am. Chem. Soc.* **2019**, *141*, 11651.

(30) Gómez, R.; Orts, J. M.; Álvarez-Ruiz, B.; Feliu, J. M. Effect of Temperature on Hydrogen Adsorption on Pt(111), Pt(110), and Pt(100) Electrodes in 0.1 M HClO4. *J. Phys. Chem. B* **2004**, *108*, 228.

(31) Ross, P. N. Hydrogen chemisorption on Pt single crystal surfaces in acidic solutions. *Surface Science* **1981**, *102*, 463.

(32) Will, F. G. Hydrogen Adsorption on Platinum Single Crystal Electrodes. *J. Electrochem. Soc.* **1965**, *112*, 451.

(33) Gudmundsdóttir, S.; Skúlason, E.; Weststrate, K.-J.; Juurlink, L.; Jónsson, H. Hydrogen adsorption and desorption at the Pt(110)-(1×2) surface: experimental and theoretical study. *PCCP* **2013**, *15*, 6323.

(34) Karlberg, G. S.; Jaramillo, T. F.; Skúlason, E.; Rossmeisl, J.; Bligaard, T.; Nørskov, J. K. Cyclic Voltammograms for H on Pt(111) and Pt(100) from First Principles. *Phys. Rev. Lett.* **2007**, *99*, 126101.

(35) Stamatakis, M.; Vlachos, D. G. A graph-theoretical kinetic Monte Carlo framework for on-lattice chemical kinetics. *J. Chem. Phys.* **2011**, *134*, 214115.

(36) Núñez, M.; Robie, T.; Vlachos, D. G. Acceleration and sensitivity analysis of lattice kinetic Monte Carlo simulations using parallel processing and rate constant rescaling. *J. Chem. Phys.* **2017**, *147*, 164103.